

UNIVERSITÀ POLITECNICA DELLE MARCHE Repository ISTITUZIONALE

Investigation of human pancreatic cancer tissues by Fourier Transform Infrared Hyperspectral Imaging

This is the peer reviewd version of the following article:

Original

Investigation of human pancreatic cancer tissues by Fourier Transform Infrared Hyperspectral Imaging / Notarstefano, Valentina; Sabbatini, Simona; Conti, Carla; Pisani, Michela; Astolfi, Paola; Pro, Chiara; Rubini, Corrado; Vaccari, Lisa; Giorgini, Elisabetta. - In: JOURNAL OF BIOPHOTONICS. - ISSN 1864-0648. - ELETTRONICO. - 13:4(2020). [10.1002/jbio.201960071]

Availability:

This version is available at: 11566/272050 since: 2024-03-26T14:37:50Z

Publisher:

Published

DOI:10.1002/jbio.201960071

Terms of use:

The terms and conditions for the reuse of this version of the manuscript are specified in the publishing policy. The use of copyrighted works requires the consent of the rights' holder (author or publisher). Works made available under a Creative Commons license or a Publisher's custom-made license can be used according to the terms and conditions contained therein. See editor's website for further information and terms and conditions.

This item was downloaded from IRIS Università Politecnica delle Marche (https://iris.univpm.it). When citing, please refer to the published version.

Publisher copyright:

Wiley - Postprint/Author's accepted Manuscript

This is the peer reviewed version of the above quoted article which has been published in final form at 10.1002/jbio.201960071. This article may be used for non-commercial purposes in accordance with Wiley Terms and Conditions for Use of Self-Archived Versions. This article may not be enhanced, enriched or otherwise transformed into a derivative work, without express permission from Wiley or by statutory rights under applicable legislation. Copyright notices must not be removed, obscured or modified. The article must be linked to Wiley's version of record on Wiley Online Library and any embedding, framing or otherwise making available the article or pages thereof by third parties from platforms, services and websites other than Wiley Online Library must be prohibited.

(Article begins on next page)

Article type: Full Article

Investigation of human pancreatic cancer tissues by Fourier Transform InfraRed HyperSpectral Imaging (FTIR-HSI)

Valentina Notarstefano^{†,1}, Simona Sabbatini^{†,2}, Carla Conti², Michela Pisani², Paola Astolfi², Chiara Pro¹, Corrado Rubini³, Lisa Vaccari⁴, and Elisabetta Giorgini^{*,1}

¹ Department of Life and Environmental Sciences, Università Politecnica delle Marche, via Brecce Bianche, 60131 Ancona, Italy

² Department of Materials, Environmental Sciences and Urban Planning, Università Politecnica delle Marche, 60131 Ancona, Italy

³ Department of Biomedical Sciences and Public Health, Università Politecnica delle Marche, 60126 Ancona, Italy

⁴Elettra Sincrotrone Trieste, SISSI Beamline, 34149 Basovizza, Trieste, Italy

*Correspondence:

Elisabetta Giorgini, Department of Life and Environmental Sciences, Università Politecnica delle Marche, via Brecce Bianche, 60131 Ancona, Italy

E-mail: e.giorgini@univpm.it

KEYWORDS: Fourier transform infrared hyperspectral imaging, pancreatic ductal adenocarcinoma, pancreatic neuroendocrine tumors, spectral biomarkers, multivariate analysis

This article has been accepted for publication and undergone full peer review but has not been through the copyediting, typesetting, pagination and proofreading process, which may lead to differences between this version and the Version of Record. Please cite this article as doi: 10.1002/jbio.201960071

[†] V.N. and S.S. equally contributed to this work.

Abstract

FTIR-HSI (Fourier-Transform InfraRed HyperSpectral Imaging) provides hyperspectral images containing both morphological and chemical information. It is widely applied in the biomedical field to detect tumor lesions, even at the early stage, by identifying specific spectral biomarkers. Pancreatic neoplasms present different prognoses and are not always easily classified by conventional analyses. In this study, tissue samples with diagnosis of pancreatic ductal adenocarcinoma and pancreatic neuroendocrine tumor were analyzed by FTIR-HSI and the spectral data compared with those from healthy and dysplastic samples. Multivariate/univariate approaches were complemented to hyperspectral images, and definite spectral markers of the different lesions identified. The malignant lesions were recognizable both from healthy/dysplastic pancreatic tissues (high values of phospholipids and triglycerides with shorter, more branched and less unsaturated alkyl chains) and between each other (different amounts of total lipids, phosphates and carbohydrates). These findings highlight different metabolic pathways characterizing the different samples, well detectable by FTIR-HSI.

1 INTRODUCTION

Pancreatic neoplasms are the fourth leading cause of cancer death in the United States, and they are expected to become the second one in a few years [1]. Being usually diagnosed only at a very late stages of the disease progression, patients with pancreatic neoplasms have a five-year survival rate of only 6%. As a matter of fact, the relative inaccessibility of the organ, as well as the non-specific nature of the symptoms, often similar to those of chronic pancreatitis, ensure a success rate for the early-stage diagnosis of only 10% [1,2]. As a result, only 20% of discovered pancreatic cancers are treatable with surgery.

The pancreatic ductal adenocarcinoma (PDAC) and the pancreatic neuroendocrine tumor (PNET) are the main types of neoplasms that can arise in the pancreas. Due to their different

origin, starting from exocrine and neuroendocrine cells respectively, and prognosis, partly related to various tumor grades, a reliable and definitive diagnosis is mandatory, especially for choosing the most appropriate chemotherapy treatment. PDAC is the most common pancreatic malignancy, representing over 90% of all pancreatic neoplasia; it frequently metastasizes in liver or lymph nodes, forming microscopic glands, that can grow enough to invade nerves [3,4]. PNETs are uncommon pancreatic tumors that account for 1 to 5% of all pancreatic neoplasms [5,6]. All PNETs are potentially malignant neoplasms, although the rate of malignancy varies according to the different tumor grades. In general, these neoplasms are slow-growing, with a survival period varying from 2 to 10 years from the time of diagnosis [5]. Even if immunohistochemistry can aid in their differential diagnosis, it alone cannot predict the tumor behavior without uncertainty.

Fourier transform infrared hyperspectral imaging (FTIR-HSI) has been widely applied in the last decade in biomedical field and in cancer research for detecting the presence of malignant tumors at micrometric scale and, as further extent, for identifying specific spectral biomarkers for their unambiguous classification [7]. By hyperspectral imaging of specific areas of tissue samples, it is possible to achieve a morpho-chemical correlation between histological and vibrational analysis [8–10]. The potential offered by FTIR-HSI to obtain relevant and punctual biomolecular information at molecular level and to detect changes in the biochemical composition and conformation of the most relevant biomolecules on the same sample and at the same time has been already reported in previous studies [11–14], investigating prostate [15], cervix [16,17], breast [18,19], colon [20,21], lung [22], thyroid [23], and skin [24] tumoral lesions. In some cases, the FTIR-HSI approach played a key role in detecting early stages of inflammatory and malignant diseases, helping to gain a deeper understanding of the etiologic nature of different pathologies, even before any detectable morphological evidence [14,15].

In the present study, biopsy samples of PDAC and PNET were analyzed by FTIR-HSI. The vibrational features of these tumoral lesions were defined and compared with those of dysplastic and healthy pancreatic tissues by means of both multivariate and univariate analyses, and appropriate spectral biomarkers able to differentiate among the different lesions were identified.

2 EXPERIMENTAL

2.1 Sample collection and preparation

The study was approved by the local Ethics Committee in full accordance with the ethical principles for medical research involving human subjects, including The Code of Ethics of the World Medical Association (Declaration of Helsinki, 2013). Samples were collected from pancreas biopsies, performed with diagnostic purposes on consenting patients who did not receive any previous pharmaceutical treatment. All patients signed informed consent to participate to this research.

Based on a preliminary classification carried out according to World Health Organization guidelines by comparing clinical, radiological, and histological outcomes, samples were divided as follows: n.2 samples of healthy pancreatic tissue, considered as the control group (CTRL); n.3 samples of dysplastic pancreatic tissue (PDy); n.3 samples of pancreatic neuroendocrine tumor (PNET), and n.3 samples of pancreatic ductal adenocarcinoma (PDAC). For each sample, six adjacent sections (10-μm thick) were cut by using a cryomicrotome set at -20°C (Microm HM 505 N, GmbH, Walldorf, Germany) and alternatively deposited onto glass slides for histological examination and CaF₂ optical windows (1-mm thick, 13-mm

diameter) for infrared analysis. The latter samples were air-dried for 30 min without any fixation process [8].

2.2 Histological Analysis

Three sections for each sample were stained with Mayer's Hematoxylin and Eosin Y (Sigma-Aldrich, Milano, Italy) and analyzed by a Zeiss Axio Imager.A2 (Oberkochen, Germany) microscope equipped with a combined color digital camera Axiocam 503 (Zeiss).

2.3 FTIR-HSI measurements and data analysis

FTIR-HSI measurements were carried out at the Chemical and Life Science branch of the infrared Beamline SISSI, Elettra Sincrotrone Trieste (Trieste, Italy), using a Hyperion 3000 Vis–IR microscope equipped with a liquid nitrogen-cooled bidimensional Focal Plane Array (FPA) detector coupled with a Vertex 70v interferometer (Bruker Optics GmbH, Ettlingen, Germany). The 64X64 pixel bidimensional FPA detector let simultaneously acquire 4,096 spectra.

Three sections were analyzed for each sample. Following pathologist's suggestions, specific areas were selected, on which the IR images (~164x164 µm²) were acquired in transmission mode, using a 15X condenser/objective, in the 4000-900 cm⁻¹ spectral region (spectral resolution 4 cm⁻¹), averaging 256 scans. IR images were acquired at room temperature; each map acquisition lasted about 5 minutes. Background spectra were obtained on clean regions of CaF₂ optical windows with the same acquisition parameters. During all measurements, the interferometer was kept in vacuum, while the microscope chassis was purged with nitrogen flow. Raw IR images were corrected for the contribution of atmospheric CO₂ and water vapor and vector normalized in the entire spectral range for avoiding artifacts induced by local

thickness variations by Atmospheric Compensation and Vector Normalization routines of OPUS 7.1 software (Bruker Optics GmbH, Ettlingen, Germany).

For the rough evaluation of the spatial distribution and the relative amount of lipids, proteins, phosphate groups (mainly of phospholipids and nucleic acids) and carbohydrates within the mapped regions, false color images were generated by integrating IR images in the following spectral regions: 2995–2828 cm⁻¹ (vibrational modes of lipid alkyl chains, LIP), 1720-1480 cm⁻¹ (vibrational modes of peptide linkage, PRT), and 1175-1000 cm⁻¹ (vibrational modes of lipid and nucleic acid phosphates and carbohydrates, PH-CARBO). The exact wavenumbers of all the vibrational modes associated with lipids, proteins, phosphates and carbohydrates are reported in Table 1.

For each IR image, ~100 spectra have been selected as representative of the experimental groups, addressing the choice on the base of the histological analysis of the adjacent sections. The extracted spectra, named pre-processed spectra from here on, did not show scattering background and spectral artefacts, hence they only required two-points baseline linear fitting and vector normalization. Then, they were integrated under the above-defined spectral regions by using the Integration Mode B (OPUS 7.1). Integrated areas were used to calculate the band area ratios LIP/TBM, PRT/TBM and PH-CARBO/TBM, TBM (overall Tissue BioMass) being the sum of the integrated areas in the regions 2995–2828 cm⁻¹ and 1781–989 cm⁻¹.

To highlight the group segregation, second derivatives of pre-processed spectra of all the experimental groups (Savitzky–Golay filter, 9-points smoothing) were submitted to Principal Component Analysis (PCA), by exploiting the 'Principal Component Analysis for Spectroscopy' tool in OriginPro 2018b software (OriginLab Corporation, Northampton, MA). Furthermore, PCA was coupled with linear discriminant analysis (LDA). First, PCA was used to reduce redundant information from the spectral dataset, by describing each spectrum with a

selected subset of PCs explaining 95% of cumulative variance; then, the reduced spectra were

used as input variables for LDA (OriginPro 2018b, OriginLab Corporation, Northampton, MA) [25,26].

Finally, to better highlight the intergroup spectral variations, the pair-wise PCA of second derivatives of pre-processed spectra of all the experimental groups was performed (CTRL-PDy, CTRL-PDAC, PDy-PNET, PDy-PDAC and PNET-PDAC); PC scores and loadings were considered.

The average absorbance spectra of CTRL, PDy, PNET and PDAC samples were calculated from pre-processed spectra, together with their corresponding standard deviation SD (Averaging routine, OPUS 7.1). Spectra were interpolated and curve fitted in the 3050-2800 cm⁻¹, 1770-1350 cm⁻¹, and 1350-900 cm⁻¹ spectral regions, upon straight baseline correction and vector normalization. For each spectral interval, the number and position of the underlying bands were identified by second derivative minima analysis and fixed during fitting procedure with Gaussian functions (GRAMS/AI 9.1, Galactic Industries, Inc., Salem, NH). The position of the selected underlying bands is reported in Table 1, together with the corresponding vibrational modes and possible biochemical assignments. The integrated areas of the band components were used to calculate specific band area ratios (see Results and Discussion section).

2.4 Statistical Analysis

Normally distributed data deriving from integration and curve fitting procedures were presented as mean±S.D. Significant differences between experimental groups were determined by means of a factorial analysis of variance (one-way ANOVA), followed by Tukey's multiple comparisons test, using the statistical software package Prism6 (Graphpad Software, Inc. USA). Significance was set at P<0.05. The statistical software OriginPro 2018b (OriginLab Corporation, Northampton, MA) was used.

3 RESULTS AND DISCUSSION

neuroendocrine tumor (PNET), dysplastic (PDy) and healthy (CTRL) pancreatic tissues were analyzed by FTIR-HSI with the aim to: (1) characterize the vibrational features of the two pancreatic neoplasms PNET and PDAC, and (2) identify appropriate spectral biomarkers for their reliable discrimination, also with respect to dysplastic and healthy pancreatic samples. To achieve these goals, the IR images of the different experimental groups were analyzed by multivariate and univariate procedures, letting correlate the spectral features of each experimental group to definite biochemical changes characteristic of the different lesions. Microscopy images of representative sections (H&E stained) of CTRL, PDy, PNET, and PDAC tissue samples are reported in Figure 1a, together with false color images representing the spatial distribution of lipids (LIP), proteins (PRT), and phosphates and carbohydrates (PH-CARBO) within representative mapped areas (Figure 1b). The images suggest what confirmed by the univariate analysis on selected pre-processed spectra (Figure 1c): with respect to CTRL samples, significant lower amounts of lipids (measured against the total tissue biomass, LIP/TBM band area ratio) were observed in PDy and PNET, while a slighter but statistically significant increment was detected in PDAC; as regards proteins (PRT/TBM band area ratio), no statistically significant differences were observed in PDy and PNET, while only PDAC displayed a small but statistically significant increase; the relative amount of phosphates and carbohydrates (PH-CARBO/TBM band area ratio) was significantly higher

Biopsy samples of human pancreatic ductal adenocarcinoma (PDAC), pancreatic

To further highlight the spectral features characterizing each pancreatic lesion, the PCA-LDA analysis was performed on CTRL, PDy, PNET, PDAC pre-processed spectra (Figure 2). The PC1-PC2 score plot showed no segregation between CTRL and PDy spectra, a partial

in PNET, lower in PDAC and similar in PDy.

segregation of PDAC with respect to CTRL and PDy, and a clear segregation of PNET with respect to all the other experimental groups (Figure 2a). The segregation pattern emerges more clearly from PCA-LDA score plot (Figure 2b). The one-dimensional score plots of LD1 and LD2 confirmed the importance of LD1 in discriminating PNET from CTRL, PDy and PDAC groups (Figure 2c), and of LD2 in separating spectra of PNET and PDAC (both malignant lesions) from CTRL and PDy (respectively healthy and dysplastic tissues) (Figure 2d).

In order to provide precise information according the spectral markers discriminating among the experimental groups, PCA was also performed in a pair-wise manner (Figure 3). Despite the complete superimposition of CTRL and PDy spectra in total PCA (Figure 2), the pair-wise PCA highlighted for these two groups a partial segregation along PC1 axis (Figure 3a). In addition, a complete segregation was obtained for both CTRL-PNET (Figure 3b) and CTRL-PDAC (Figure 3c). PNET clearly segregates from PDy and PDAC (Figures 3d,f), while PDAC partially overlaps with PDy (Figure 3e). By the analysis of PC1 loadings (Figures 3g-l), spectral modifications were revealed in the entire spectral range; in particular, the following regions resulted to play a different role depending on the considered pair: 3050-2800 cm⁻¹ (Zone 1, representative of lipids), 1760-1700 cm⁻¹ (Zone 2, representative of triglycerides, phospholipids and DNA), 1700-1600 cm⁻¹ (Zone 3, representative of Amide I of cellular proteins), 1500-1400 cm⁻¹ (Zone 4, representative of lipid aliphatic chains and collagen) and 1150-1050 cm⁻¹ (Zone 5, representative of phosphates in nucleic acids and phospholipids, and carbohydrates).

To implement the information from loadings of second derivative spectra, a matching with data retrieved from absorbance spectra was performed. To this purpose, the average absorbance spectra of CTRL, PDy, PNET and PDAC samples and their corresponding average \pm SD spectra were calculated (Figure 4a), and fitted in the 3050-2800 cm⁻¹, 1770-1350 cm⁻¹, and 1350-900 cm⁻¹ regions, based on the position of minima of second derivative

spectra (Figure 4b). Specific band area ratios were then analyzed. Regarding lipids, the band area ratios 2925/2960 (ratio between the -CH₂ and -CH₃ groups mainly of lipids, representing the length/branching of lipid aliphatic chains; Figure 5a) and 3008/2960 (ratio between the =CH and -CH₃ groups mainly of lipids, representing the degree of unsaturation of lipid aliphatic chains; Figure 5b) were analyzed. For both ratios, lower values (P<0.05) were observed in both dysplastic and malignant pancreatic lesions (PDy, PNET and PDAC) with respect to CTRL. In addition, in PNET and PDAC, an increase (P<0.05) of the band area ratio 1746/AmI (ratio between the C=O ester moieties of triglycerides/phospholipids and the Amide I band of proteins, representing the relative amount of triglycerides and phospholipids with respect to cellular proteins; Figure 5c) was also observed. The band area ratios 1460/AmI and 1396/AmI correspond to the ratios between the CH₃ groups in proteins side chains and, to a minor extent, in cellular lipids and the Amide I band of proteins (Figure 5d,e). In PDAC and PDy samples, both these ratios showed higher values with respect to CTRL (P<0.05), while no changes were observed in PNET. The attribution of these two bands is not univocal, since they are associated to bending modes of aliphatic chains in proteins and lipids. Since PDAC has a dense fibrotic stroma, mainly composed of collagen, which impedes the tumor perfusion and the delivery of anticancer drugs [33], it seems reasonable to associate the detected spectral changes to collagen accumulation. The band at 1170 cm⁻¹, associated to nonhydrogen bonds of C—O stretching vibrations of glycosylated cellular molecules [34], is reported in literature as diagnostic of malignancy [30]. The correlation of this parameter with the impairment of glycosylation and dephosphorylation/phosphorylation processes in tumors was confirmed by the higher values of the band area ratio 1170/1240 (ratio between C—O groups of cellular molecules and the phosphate groups of phospholipids and nucleic acids; Figure 5f) found in the two malignant lesions PNET and PDAC with respect to CTRL and PDy (P<0.05). Regarding the band area ratios 1116/1240 (ratio between C2'-OH group of RNA and NTPs and phosphate groups mainly in nucleic acids and phospholipids; Figure 5g) and 1083/1240 (ratio between phosphate groups of nucleic acids to nucleic acids and phospholipids; Figure 5h), PDy and PDAC showed values similar to CTRL, while PNET displayed twice the value of CTRL (P<0.05). The band area ratio 1048/1240 (ratio between the C-O-H groups in carbohydrates and phosphate groups, mainly in phospholipids, representing the amount of carbohydrates with respect to phosphate groups in phospholipids; Figure 5j) showed similar values in CTRL, PNET and PDy, while PDAC displayed the lowest amount (P<0.05). Finally, a decrease of the band area ratio 1712/AmI (ratio between the carbonyl groups of DNA and phosphate groups mainly in phospholipids; Figure 5i) was found (P<0.05) both in PNET and PDAC, while no differences were observed between CTRL and PDy samples.

Summarizing, the dysplastic sample PDy displayed a set of spectral features closer to the healthy pancreatic tissue (CTRL), with no differences in phosphates and carbohydrates (PH-CARBO maps; PH-CARBO/TBM, 1170/1240, 1048/1240, 1116/1240 and 1083/1240 ratios), total proteins (PRT maps; PRT/TBM ratios), and triglycerides and phospholipids (1746/1657 ratio). Only a slight increment of collagen (1460/1657 and 1396/1657 ratios) was detected, together with a lower amount of total lipids (LIP maps) with shorter and more branched lipid alkyl chains (2925/2960 ratio) and a lower degree of unsaturation (3008/2960 ratio).

Conversely, the two malignant tumor lesions PNET and PDAC resulted clearly distinguishable with respect to both CTRL and between each other, since they do not always share a similar trend. With respect to CTRL, they both presented a relevant increase of the 1170/1240 ratio, associated with the onset of tumoral lesions [35–37]; moreover, they shared the same lipid composition, with a higher amount of phospholipids and triglycerides (1746/1657 ratio), shorter and more branched alkyl chains (2925/2960 ratio) with a lower degree of unsaturation (3008/2960 band area ratio) with respect to CTRL. These findings agree with the known impairment of lipid metabolism associated with the onset of a pathological condition, including the modulation of lipogenesis characterizing tumor

development [38,39]. Conversely, an opposite trend in the relative amount of total lipids was observed, lower in PNET and higher in PDAC (LIP map and LIP/TBM ratio). Regarding phosphates and carbohydrates, PDAC was characterized by lower amounts of carbohydrates (PH-CARBO map; PH-CARBO/TBM and 1048/1240 ratios), probably due to the higher consumption by tumoral cells [40], while in PNET an increase of phosphate groups (PH-CARBO map; PH-CARBO/TBM, 1116/1240 and 1083/1240 ratios) was found [40]. The spectral component at 1116 cm⁻¹ is diagnostic of RNA and NTPs, and it could be related to the cellular transcriptional activity [32].

The prominent stromal compartment characterizing PDAC was confirmed by the increment of total proteins (PRT map) and collagen (1460/1657 and 1396/1657 ratios) [41]. Conversely, no differences were observed in the protein pattern of PNET (PRT map; PRT/TBM, 1460/1657 and 1396/1657 ratios), consistently with its known structure, rich in small vessels and poor in fibrotic stroma [42].

4 CONCLUSIONS

In the present study, we demonstrate that FTIR-HSI provides a set of distinctive biochemical markers characterizing pancreatic ductal adenocarcinoma and pancreatic neuroendocrine tumor, also with respect to healthy and dysplastic samples. Given the low rates of successful early diagnosis of pancreatic tumors, and the subsequent low percentages of cases treatable with surgery, the finding of a specific set of spectral biomarkers (mainly related to lipid and carbohydrate metabolism, and cell transcriptional activity), able to discriminate different pancreatic lesions let gain a deeper knowledge on their different nature, even before any morphological evidence can be detected.

In conclusion, this feasibility study suggests a possible future coupling of FTIR-HSI with routinely applied immunohistochemical and histological procedures in order to improve the percentage of early diagnoses.

Acknowledgments This study was supported by the Grant of the Polytechnic University of Marche "Ricerca Scientifica di Ateneo 2017 and 2018". Authors acknowledge Elettra Sincrotrone Trieste S.C.p.A. for the access to SISSI beamline experimental facility (Proposal Number 20177047).

CONFLICT OF INTEREST

The authors declare no financial or commercial conflict of interest.

REFERENCES

- [1] American Cancer Society, Cancer Facts & Figures 2019,

 https://www.cancer.org/research/cancer-facts-statistics/all-cancer-facts-figures/cancer-facts-figures-2019.html.
- [2] T. P. Yeo, R. H. Hruban, S. D. Leach, R. E. Wilentz, T. A. Sohn, S. E. Kern, C. A. Iacobuzio-Donahue, A. Maitra, M. Goggins, M. I. Canto, R. A. Abrams, D. Laheru, E. M. Jaffee, M. Hidalgo and C. J. Yeo, *Curr. Probl. Cancer*, 2002, 26, 176.
- [3] W. R. Lloyd, R. H. Wilson, S. Y. Lee, M. Chandra, B. McKenna, D. Simeone, J. Scheiman and M.-A. Mycek, *Biomed. Opt. Express*, **2014**, *5*, 9.
- [4] A. S. Takhar, P. Palaniappan, R. Dhingsa and D. N. Lobo, *BMJ*, **2004**, *329*, 668.
- [5] G. Low, A. Panu, N. Millo and E. Leen, *RadioGraphics*, **2011**, *31*, 993.
- [6] G. Klöppel and M. Anlauf, *Pathol. Case Rev.*, **2006**, *11*, 256.
- [7] H. Sreedhar, V. K. Varma, P. L. Nguyen, B. Davidson, S. Akkina, G. Guzman, S. Setty,

- A. Kajdacsy-Balla and M. J. Walsh, J. Vis. Exp., 2015, 1.
- [8] E. Giorgini, S. Sabbatini, C. Conti, C. Rubini, R. Rocchetti, M. Re, L. Vaccari, E. Mitri and V. Librando, *J. Biomed. Opt.*, **2015**, *20*, 125003.
- [9] E. Giorgini, G. Tosi, C. Conti, S. Staibano, G. Ilardi and S. Sabbatini, *Spectrochim. Acta Part A Mol. Biomol. Spectrosc.*, **2015**, *141*, 99.
- [10] M. Z. Kastyak-Ibrahim, M. J. Nasse, M. Rak, C. Hirschmugl, M. R. Del Bigio, B. C. Albensi and K. M. Gough, *Neuroimage*, 2012, 60, 376.
- [11] A. Kallenbach-Thieltges, F. Großerüschkamp, A. Mosig, M. Diem, A. Tannapfel and K. Gerwert, *J. Biophotonics*, **2013**, *6*, 88.
- [12] M. J. Baker, E. Gazi, J. H. Shanks, P. Gardner, N. W. Clarke, M. D. Brown, J. H. Shanks, P. Gardner and N. W. Clarke, *Br. J. Cancer*, **2008**, *99*, 1859.
- [13] G. E. Menzies, H. R. Fox, C. Marnane, L. Pope, V. Prabhu, S. Winter, A. V. Derrick and P. D. Lewis, *Transl. Res.*, **2014**, *163*, 19.
- [14] K. Badizadegan, V. Backman, C. W. Boone, C. P. Crum, R. R. Dasari, I. Georgakoudi, K. Keefe, K. Munger, S. M. Shapshay, E. E. Sheetse and M. S. Feld, *Faraday Discuss.*, 2004, 126, 265.
- [15] M. J. Baker, E. Gazi, J. H. Shanks, P. Gardner and N. W. Clarke, *Br. J. Cancer*, 2008, 99, 1859.
- [16] B. R. Wood, M. Kiupel and D. McNaughton, Vet. Pathol., 2014, 51, 224.
- [17] Y. Jusman, N. A. Mat Isa, S.-C. Ng, K. Hasikin and N. A. Abu Osman, *J. Biomed. Opt.*,2016, 21, 075005.
- [18] F. Elmi, A. F. Movaghar, M. M. Elmi, H. Alinezhad and N. Nikbakhsh, *Spectrochim. Acta Part A Mol. Biomol. Spectrosc.*, **2017**, *187*, 87.
- [19] J. Backhaus, R. Mueller, N. Formanski, N. Szlama, H.-G. Meerpohl, M. Eidt and P. Bugert, *Vib. Spectrosc.*, **2010**, *52*, 173.
- [20] S. Gurunathan, M. Qasim, C. Park, H. Yoo, J.-H. Kim and K. Hong, Int. J. Mol. Sci.,

- **2018**, 19, 2269.
- [21] E. Kaznowska, J. Depciuch, K. Szmuc and J. Cebulski, *J. Pharm. Biomed. Anal.*, **2017**, 134, 259.
- [22] E. Kaznowska, K. Łach, J. Depciuch, R. Chaber, A. Koziorowska, S. Slobodian, K. Kiper, A. Chlebus and J. Cebulski, *Infrared Phys. Technol.*, 2018, 89, 282.
- [23] J. Depciuch, A. Stanek-Widera, D. Lange, M. Biskup-Frużyńska, J. Stanek-Tarkowska, W. Czarny and J. Cebulski, *Spectrochim. Acta Part A Mol. Biomol. Spectrosc.*, 2018, 204, 18.
- [24] D. Sebiskveradze, B. Bertino, V. Gaydou, A.-S. Dugaret, M. Roquet, D. E. Zugaj, J. J.Voegel, P. Jeannesson, M. Manfait and O. Piot, *J. Biophotonics*, 2018, *11*, e201700380.
- [25] C. Morais and K. Lima, J. Braz. Chem. Soc., 2017, 29, 472.
- [26] C. L. M. Morais, R. F. Shore, M. G. Pereira and F. L. Martin, *ACS Omega*, **2018**, *3*, 13399.
- [27] C. Petibois and G. Déléris, Trends Biotechnol., 2006, 24, 455.
- [28] A. N. A. Aryee, F. R. van de Voort and B. K. Simpson, *Process Biochem.*, **2009**, *44*, 401.
- [29] B. Vileno, S. Jeney, A. Sienkiewicz, P. R. Marcoux, L. M. Miller and L. Forró, Biophys. Chem., 2010, 152, 164.
- [30] A. C. S. Talari, M. A. G. Martinez, Z. Movasaghi, S. Rehman and I. U. Rehman, *Appl. Spectrosc. Rev.*, **2017**, *52*, 456.
- [31] K. Belbachir, R. Noreen, G. Gouspillou and C. Petibois, *Anal. Bioanal. Chem.*, **2009**, 395, 829.
- [32] P. Zucchiatti, E. Mitri, S. Kenig, F. Billè, G. Kourousias, D. E. Bedolla and L. Vaccari, *Anal. Chem.*, **2016**, 88, 12090.
- [33] M. Weniger, K. C. Honselmann and A. S. Liss, *Cancers (Basel).*, **2018**, *10*, 316.
- [34] P. T. Wong, R. K. Wong, T. A. Caputo, T. A. Godwin and B. Rigas, *Proc. Natl. Acad.*

- Sci. U. S. A., 1991, 88, 10988.
- [35] S. Caine, P. Heraud, M. J. Tobin, D. McNaughton and C. C. A. Bernard, *Neuroimage*, **2012**, *59*, 3624.
- [36] J. Kneipp, M. Beekes, P. Lasch and D. Naumann, J. Neurosci., 2002, 22, 2989.
- [37] D. Simonova and I. Karamancheva, Biotechnol. Biotechnol. Equip., 2013, 27, 4200.
- [38] C. R. Santos and A. Schulze, *FEBS J.*, **2012**, 279, 2610.
- [39] Y.-J. Chen, Y.-D. Cheng, H.-Y. Liu, P.-Y. Lin and C.-S. Wang, *Chang Gung Med. J.*,2006, 29, 518.
- [40] M. Khanmohammadi and A. B. Garmarudi, TrAC Trends Anal. Chem., 2011, 30, 864.
- [41] T. Hata, K. Kawamoto, H. Eguchi, Y. Kamada, S. Takamatsu, T. Maekawa, S. Nagaoka, D. Yamada, Y. Iwagami, T. Asaoka, T. Noda, H. Wada, K. Gotoh, A. Masamune, E. Miyoshi, M. Mori and Y. Doki, *Pancreas*, 2017, 46, 1259.
- [42] P. Capelli, G. Martignoni, F. Pedica, M. Falconi, D. Antonello, G. Malpeli and A. Scarpa, *Arch. Pathol. Lab. Med.*, **2009**, *133*, 350.

TABLE 1 Position, vibrational mode and biochemical assignment of the underlying bands as identified by curve fitting analysis of CTRL, PDy, PNET and PDAC average absorbance spectra.

Spectral range (cm ⁻¹)	Wavenumber	Vibrational mode and
	(cm ⁻¹)	biochemical assignment
3050–2800	3008	Stretching vibration of =CH groups (unsaturated aliphatic chains of lipids) [8,27]
	2960, 2866	Asymmetric and symmetric stretching vibrations of CH ₃ groups (branched aliphatic chains of lipids) [8,27]
	2925, 2853	Asymmetric and symmetric stretching vibrations of CH ₂ groups (linear aliphatic chains of lipids) [8,27]
1770–1350	1746	Stretching vibration of C=O ester moieties in triglycerides and phospholipids [28,29]
	1712	Stretching vibration of C=O groups double-helix in nucleic acids [30]
	1697, 1682, 1657, 1639, 1622, 1597	Amide I band components of proteins (AmI) [8]
	1570, 1544, 1512	Amide II band components of proteins (AmII) [8]
	1460, 1396	Bending modes of CH ₃ groups in proteins side chains (mainly collagen) and cellular lipids [31]
1350–900	1240	Asymmetric stretching vibrations of phosphate moieties mainly of phospholipids and nucleic acids [32]
	1170	Asymmetric stretching vibration of C-O- groups, prominent in malignant tissues [30]
	1116	Stretching vibration of the skeletal structure around the C2'-OH
		group of RNA and NTPs [32]
	1083	Symmetric stretching vibrations of phosphate moieties in nucleic acids [32]
	1048	Stretching vibration of C-OH groups in carbohydrates [30]

FIGURE LEGENDS

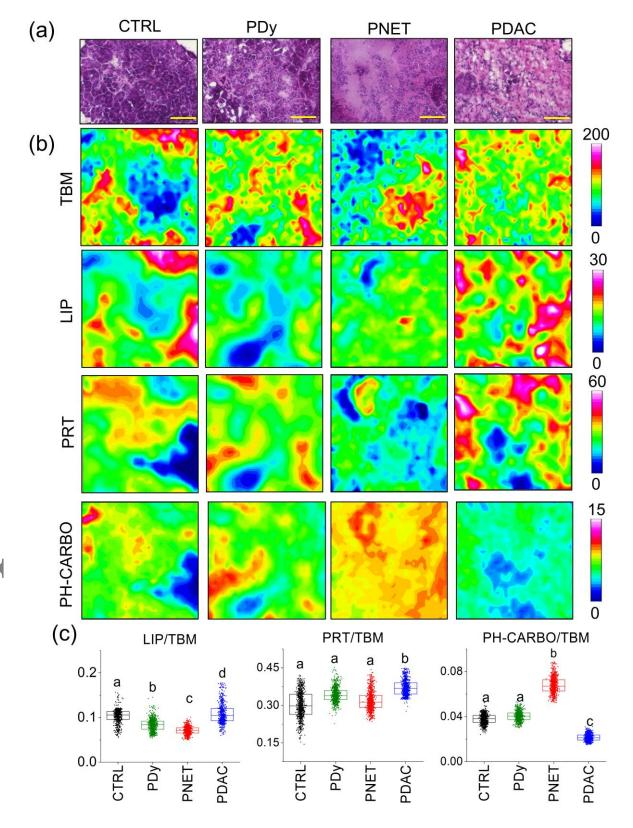
FIGURE 1 Imaging analysis of representative sections of healthy (CTRL) and dysplastic pancreatic tissues (PDy), pancreatic neuroendocrine tumor (PNET), and pancreatic ductal adenocarcinoma (PDAC). (a) Representative H&E tissue sections. Scale bars (yellow) represent 100 μm. (b) Representative IR images showing the topographical distribution of overall tissue biomass (TBM), lipids (LIP), proteins (PRT), and phosphates and carbohydrates (PH-CARBO); different color scales were used for a better interpretation of the data. (c) Statistical evaluation of the biochemical composition of CTRL, PDy, PNET, and PDAC samples in terms of lipids (LIP/TBM), proteins (PRT/TBM), and phosphates and carbohydrates (PH-CARBO/TBM). Data are reported as mean±S.D. Different letters indicate statistically significant differences among groups (P<0.05; one-way ANOVA and Tukey's multiple comparisons test).

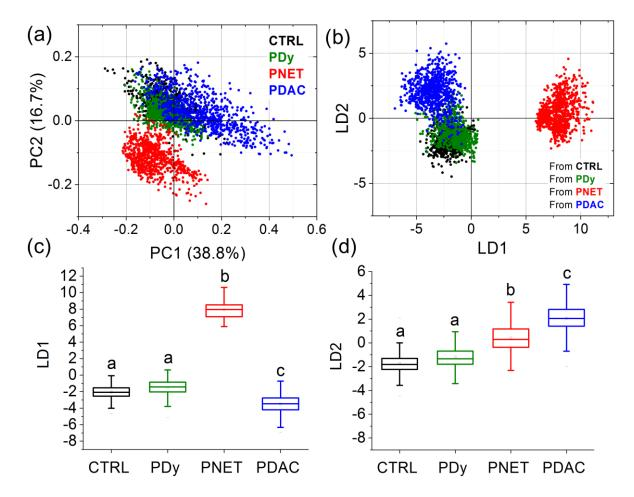
FIGURE 2 (a) PCA scores plot of CTRL, PDy, PNET, and PDAC second-derivative spectra. The percentages of variance explained by PC1 and PC2 are reported in brackets. (b) PCA-LDA scores plot of CTRL, PDy, PNET, and PDAC second-derivative spectra. LD1 and LD2 represent the first and second linear discriminant functions obtained by the canonical variables scores of PCA-LDA. One-dimensional score plots of (c) LD1 and (d) LD2. Box chart legend: center line = median; edges = 25th and 75th percentile; whiskers = standard deviation. Different letters over box charts indicate statistically significant differences among groups (P<0.05; one-way ANOVA and Tukey's multiple comparisons test).

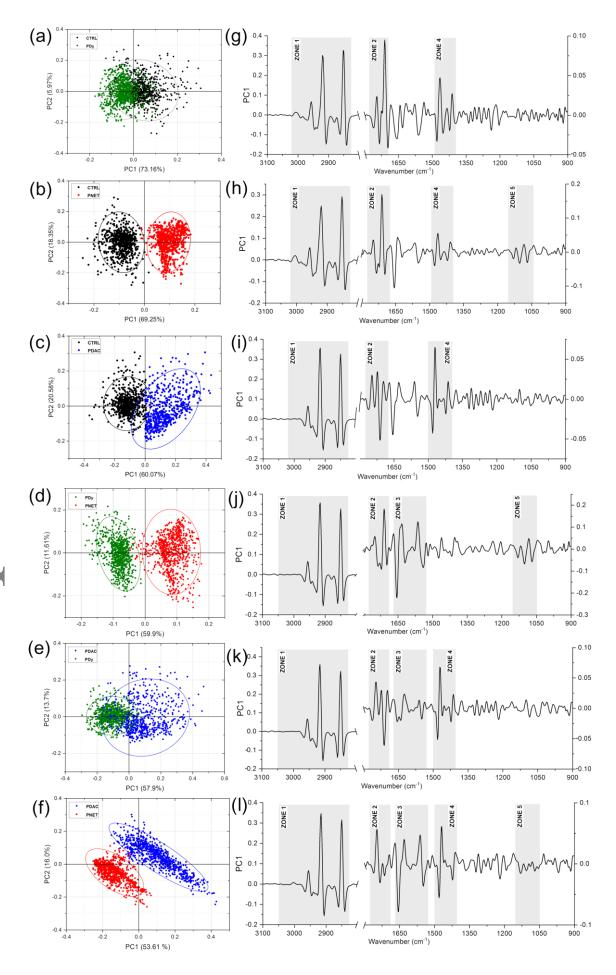
FIGURE 3 PCA scores plots of second-derivative spectra of: (a) CTRL-PDy; (b) CTRL-PNET; (c) CTRL-PDAC; (d) PDy-PNET; (e) PDy-PDAC, and (f) PNET-PDAC populations. PC1 loadings of: (g) CTRL-PDy; (h) CTRL-PNET; (i) CTRL-PDAC; (j) PDy-PNET; (k) PDy-PDAC, and (l) PNET-PDAC populations. Grey boxes indicate the regions showing the major changes in the spectral profile.

FIGURE 4 Average spectra of CTRL, PDy, PNET and PDAC samples reported in: (a) absorbance (4000-900 cm⁻¹), and (b) second derivative (3100-900 cm⁻¹) modes. The wavenumber of the most relevant peaks (corresponding to minima in second derivative spectra) is reported.

FIGURE 5 Statistical analysis of the following band area ratios calculated for CTRL, PDy, PNET and PDAC samples: (a) 2925/2960; (b) 3008/2960; (c) 1746/1657; (d) 1460/AmI; (e) 1396/AmI; (f) 1170/1240; (g) 1116/1240; (h) 1083/1240; (i) 1712/AmI; (j) 1048/1240. Data are presented as mean±S.D. Different letters over box charts indicate statistically significant differences among groups (P<0.05; one-way ANOVA and Tukey's multiple comparisons test).







This article is protected by copyright. All rights reserved.

